Supplementary Information

Defect-Engineered N-Doped Carbon Stabilizes Cu^+ Active Sites for Bifunctional CO_2 Electroreduction to CO and Formate

Pirapath Arkasalerks[a], Phongphot Sakulaue[a,b], Pongkarn Chakthranont[c], Kanokwan Kongpatpanich[d], Khanin Nueangnoraj[a*]

[a] *School of Bio-Chemical Engineering and Technology, Sirindhorn International Institute of Technology, Thammasat University, Pathum Thani, 12120, Thailand.*

[b] *Division of Chemical Engineering, Faculty of Engineering, Rajamangala University of Technology Krungthep, Bangkok 10120, Thailand.*

[c] *National Nanotechnology Center (NANOTEC), National Science and Technology Development Agency (NSTDA), Khlong Luang, Pathum Thani, 12120, Thailand*

[d] *Department of Materials Science and Engineering, School of Molecular Science and Engineering, Vidyasirimedhi Institute of Science and Technology, Rayong 21210, Thailand.*

*Corresponding author: K. Nueangnoraj (khanin@siit.tu.ac.th).

Table S1. Specific surface area (S_{BET}) and porous properties of the as-prepared carbons and composites.

sample	S_{BET} ($m^2\ g^{-1}$)	V_{total} ($cm^3\ g^{-1}$)	V_{micro} ($cm^3\ g^{-1}$)	V_{meso} ($cm^3\ g^{-1}$)
YEC	1,840	0.90	0.84	0.06
TL9	1,770	0.86	0.74	0.12
YEC/Cu-40%	855	0.47	0.40	0.07
TL9/Cu-10%	1,329	0.79	0.60	0.19
TL9/Cu-20%	970	0.57	0.46	0.11
TL9/Cu-30%	884	0.59	0.38	0.21
TL9/Cu-40%	840	0.53	0.40	0.13
TL9/Cu-50%	535	0.70	0.32	0.38

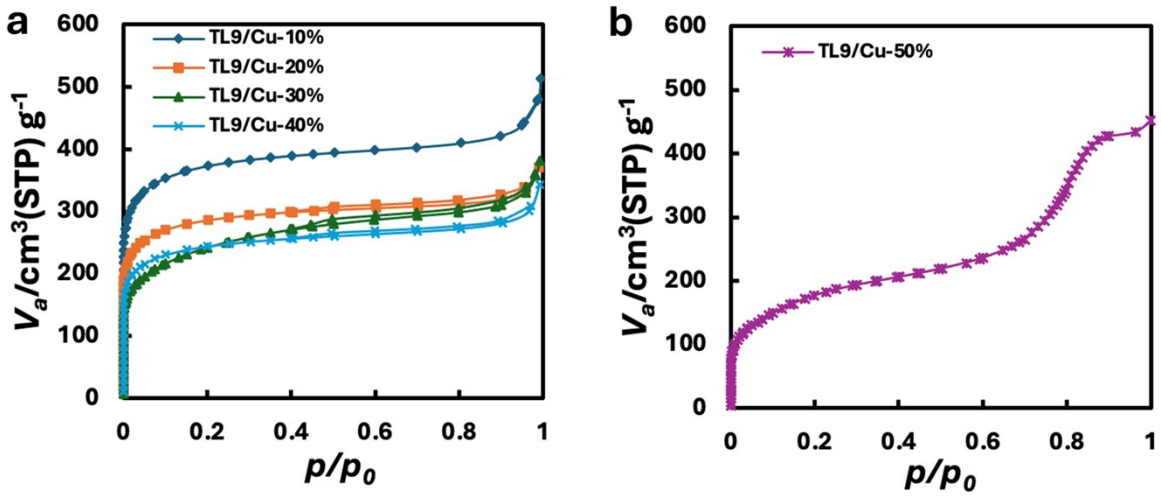

Figure S1. N_2 adsorption-desorption isotherms of (a) TL9 with Cu_2O loading from 10% to 40% and (b) TL9/Cu-50%.

Table S2. Details for the deconvolution from Raman spectra.

sample	peak	peak position	fitted area	%area	intensity	FWHM	I_D/I_G
YEC	D*	1,200.0	43,144.5	18.55	183.56	220.08	2.94
	D	1,344.9	91,663.4	39.40	513.7	163.95	
	D**	1,525.6	70,150.7	30.15	377.6	173.17	
	G	1,588.1	27,679.6	11.90	365	70.8	
TL9	D*	1,200.0	33,678.5	16.47	134.94	234.45	3.42
	D	1,344.1	89,984.3	43.99	504.11	167.69	

	D**	1,538.7	60,879.3	29.76	357.49	160	
	G	1,590.0	19,995.5	9.78	291.48	64.44	
YEC/Cu-40%	D*	1,200.0	10,450.0	20.14	41.323	237.44	3.06
	D	1,342.2	19,327.0	37.25	136.46	137.55	
	D**	1,528.7	16,102.9	31.04	90.24	171.319	
	G	1,591.9	6,004.84	11.57	87.7	62.42	
TL9/Cu-10%	D*	1,200.0	33,678.5	16.47	134.94	234.45	3.83
	D	1,344.1	89,984.3	43.99	504.11	167.69	
	D**	1,538.7	60,879.3	29.76	357.49	160	
	G	1,590.0	19,995.5	9.78	291.48	64.44	

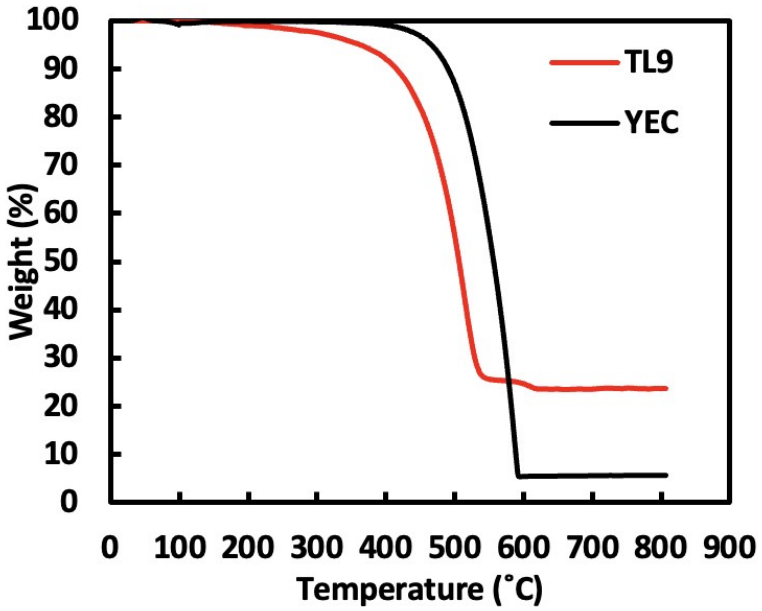

Figure S2. TGA plots of TL9 and YEC under air flow.

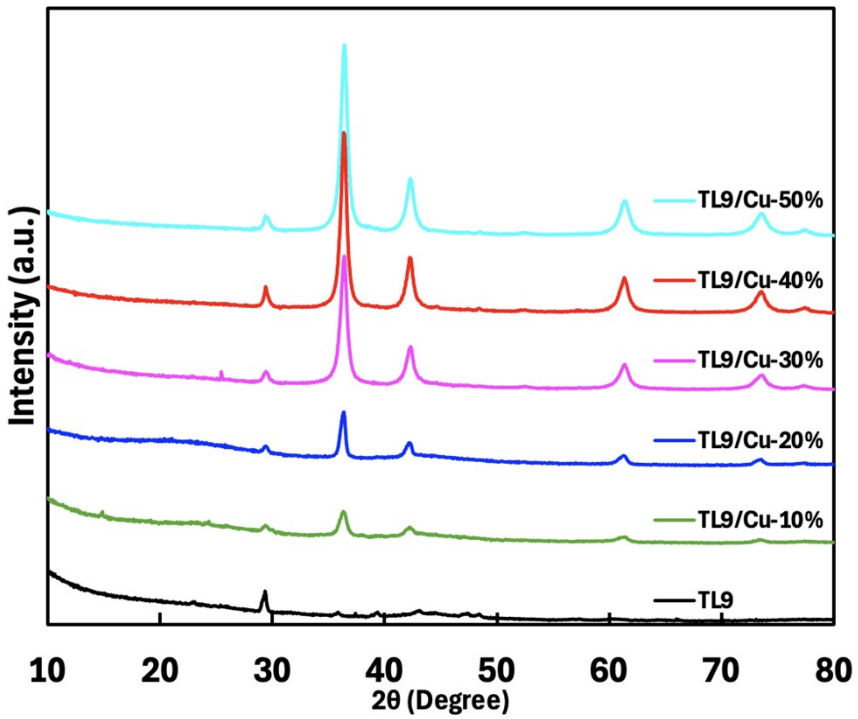

Figure S3. XRD patterns of the composites with various Cu_2O loading on TL9.

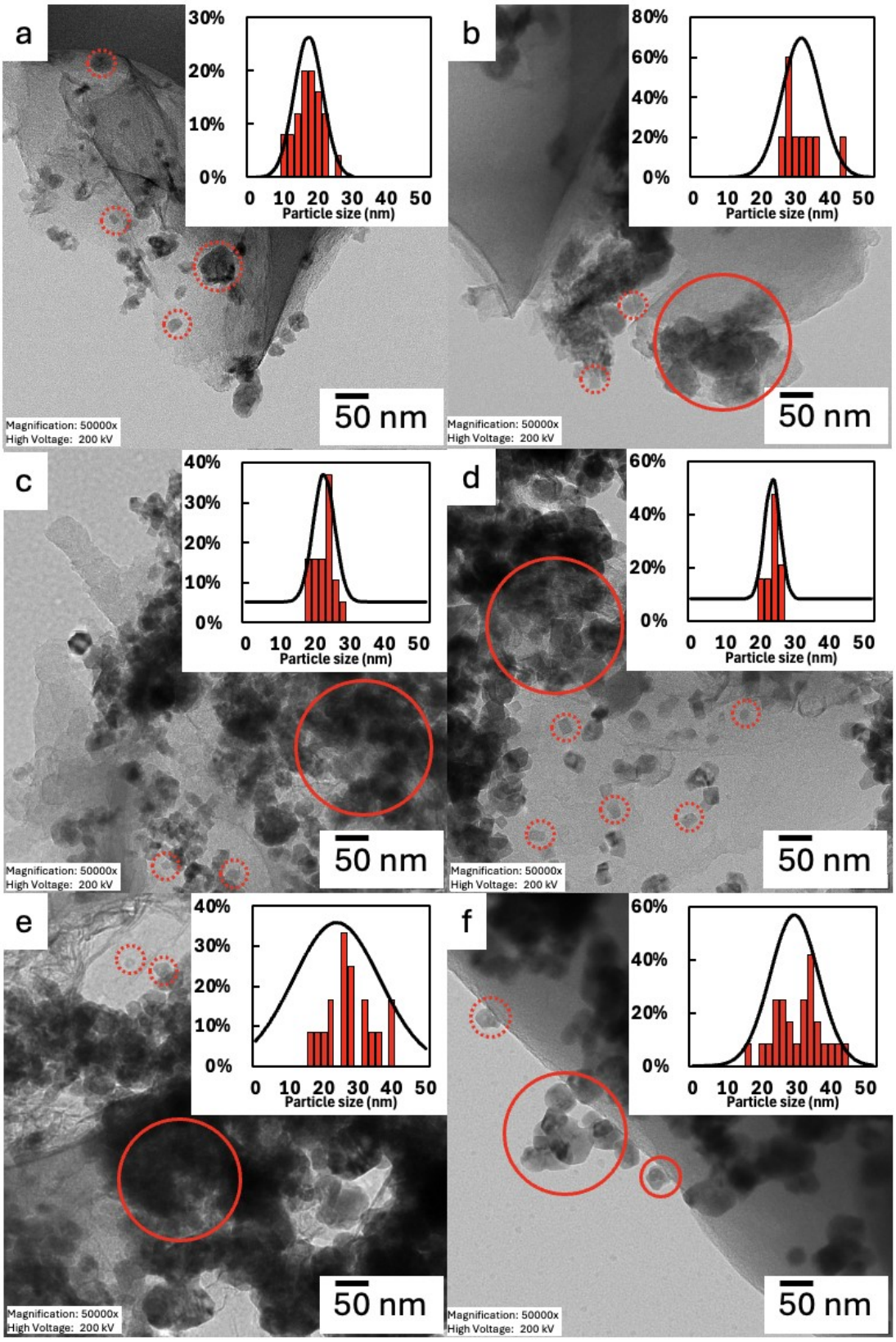
a
30%
20%
10%
0%
0 10 20 30 40 50
Particle size (nm)
50 nm
Magnification: 50000x
High Voltage: 200 kV
b
80%
60%
40%
20%
0%
0 10 20 30 40 50
Particle size (nm)
50 nm
Magnification: 50000x
High Voltage: 200 kV
c
40%
30%
20%
10%
0%
0 10 20 30 40 50
Particle size (nm)
50 nm
Magnification: 50000x
High Voltage: 200 kV
d
60%
40%
20%
0%
0 10 20 30 40 50
Particle size (nm)
50 nm
Magnification: 50000x
High Voltage: 200 kV
e
40%
30%
20%
10%
0%
0 10 20 30 40 50
Particle size (nm)
50 nm
Magnification: 50000x
High Voltage: 200 kV
f
60%
40%
20%
0%
0 10 20 30 40 50
Particle size (nm)
50 nm
Magnification: 50000x
High Voltage: 200 kV

Figure S4. TEM images of (a) TL9/Cu-10%, (b) TL9/Cu-20%, (c) TL9/Cu-30%, (d) TL9/Cu-40%, (e) TL9/Cu-50%, and (f) YEC/Cu-40% with (inset) their particle size distributions.

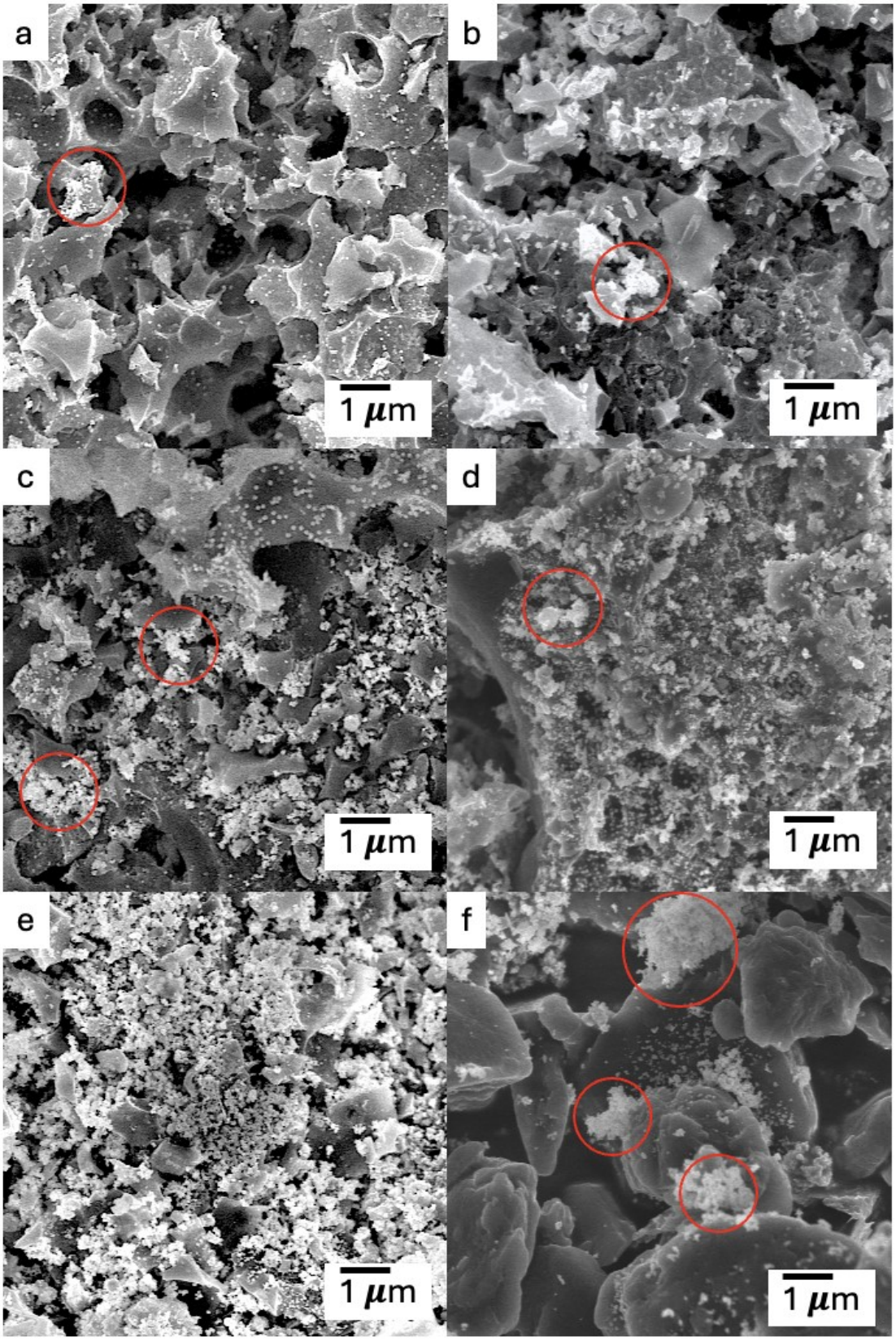

Figure S5. SEM images of (a) TL9/Cu-10%, (b) TL9/Cu-20%, (c) TL9/Cu-30%, (d) TL9/Cu-40%, (e) TL9/Cu-50%, and (f) YEC/Cu-40%.

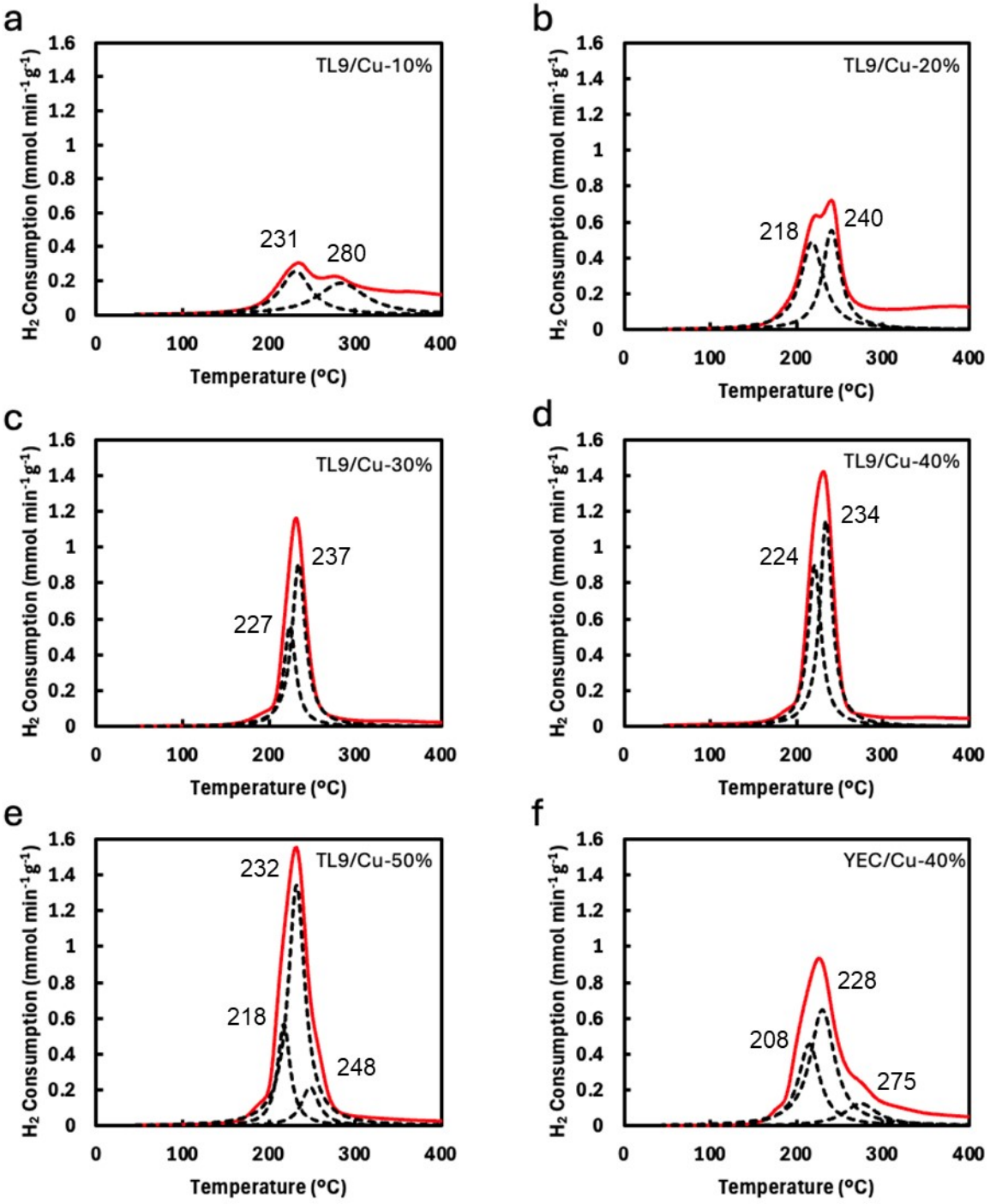

Figure S6. H_2-TPR profiles corresponded to (a) TL9/Cu-10%, (b) TL9/Cu-20%, (c) TL9/Cu-30%, (d) TL9/Cu-40%, (e) TL9/Cu-50%, and (f) YEC/Cu-40%.

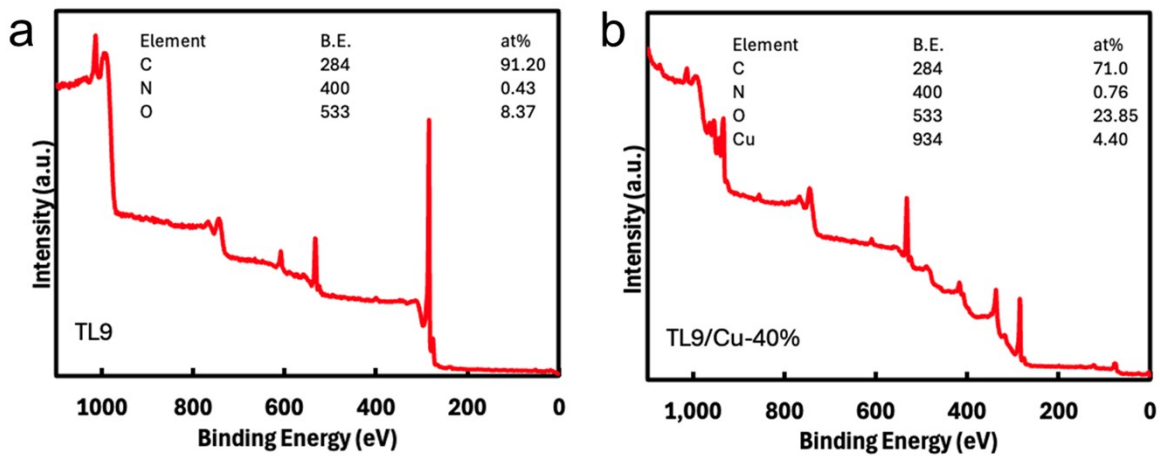

Figure S7. XPS survey spectrum of (a) TL9 and (b) TL9/Cu-40%.

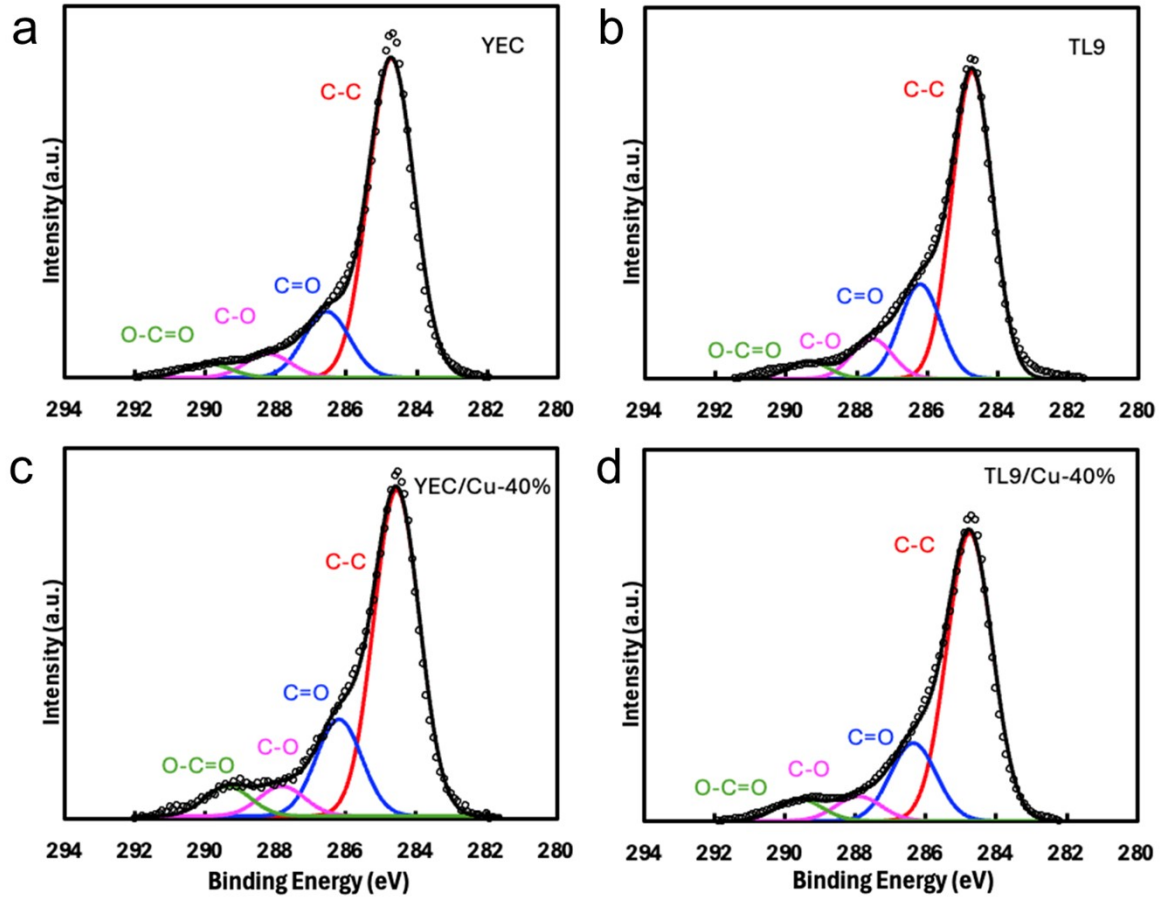

Figure S8. C 1s spectra corresponded to (a) YEC, (b) TL9, (c) YEC/Cu-40%, and (d) TL9/Cu-40%.

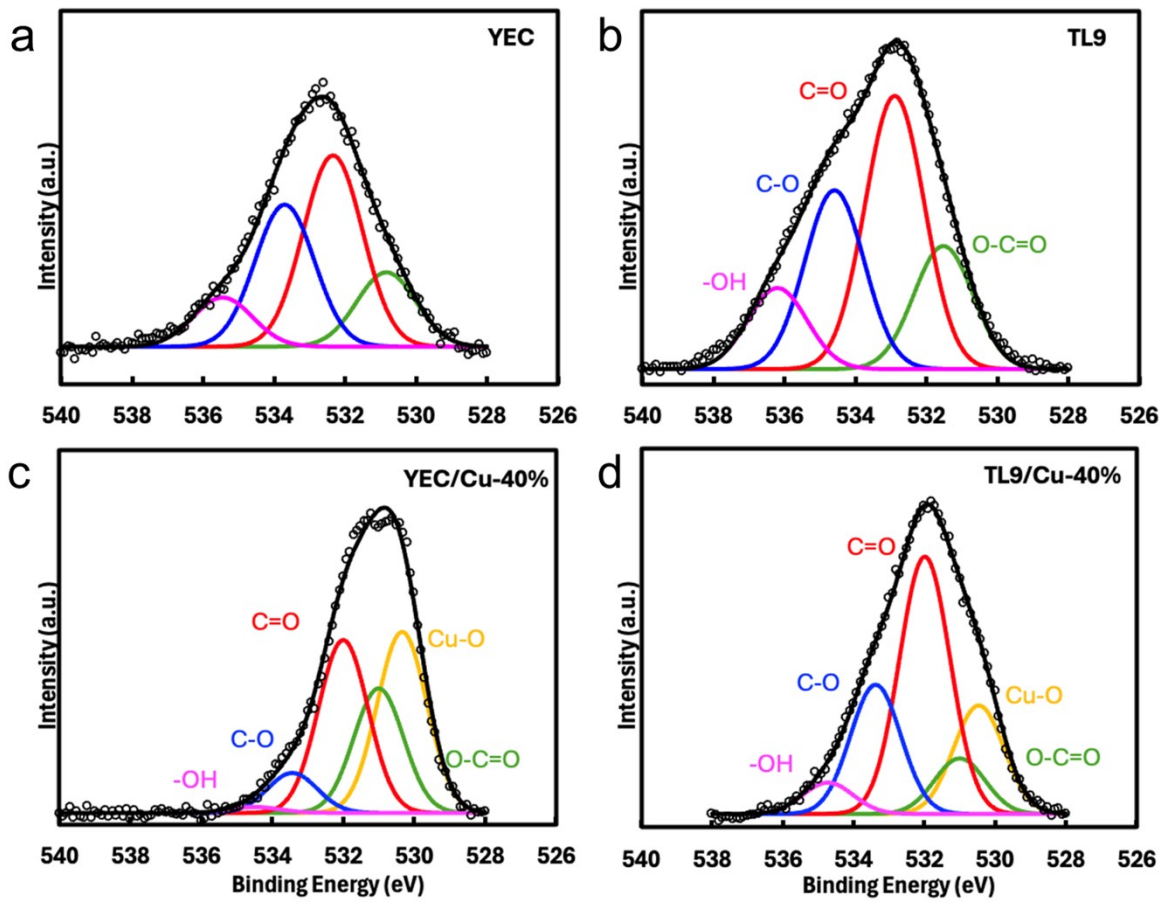

Figure S9. O 1s spectra corresponded to (a) YEC, (b) TL9, (c) YEC/Cu-40%, and (d) TL9/Cu-40%.

Table S3. Relative composition of each Cu oxidation state determined from Cu LMM region of TL9 under various Cu_2O loadings.

sample	oxidation state					
	Cu^0		Cu^+		Cu^{2+}	
	K.E. (eV)	at%	K.E. (eV)	at%	K.E. (eV)	at%
TL9/Cu-10%	-	-	916.7	88	913.1	12
TL9/Cu-20%	920.6	3	916.8	72	913.3	25
TL9/Cu-30%	919.3	14	916.7	70	913.3	16
TL9/Cu-40%	920.1	14	916.8	70	913.2	16
TL9/Cu-50%	919.1	15	916.8	72	913.2	13
YEC/Cu-40%	919.2	34	916.8	52	912.6	14

Table S4. XPS-derived atomic percentages of Cu, Cu–N_x, and nitrogen species (pyridinic-N, pyrrolic-N, and graphitic-N) for TL9 and TL9/Cu-x% catalysts.

Sample	Cu (at%)	Cu-Nx (at%)	Pyridinic-N (at%)	Pyrrolic-N (at%)	Graphitic-N (at%)
TL9			0.098	0.169	0.164
TL9/Cu-10%	1.520	0.122	0.132	0.134	0.041
TL9/Cu-20%	2.520	0.147	0.121	0.124	0.038
TL9/Cu-30%	3.930	0.205	0.144	0.065	0.016
TL9/Cu-40%	4.400	0.212	0.145	0.036	0.036
TL9/Cu-50%	9.330	0.214	0.131	0.057	0.028

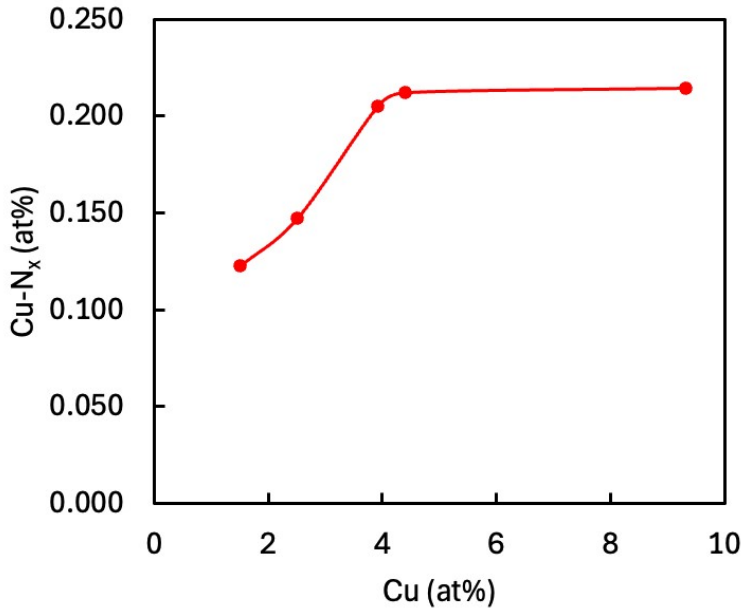

Figure S10. Correlation between Cu atomic percentage (Cu at%) and Cu–N_x derived from N 1s deconvolution.

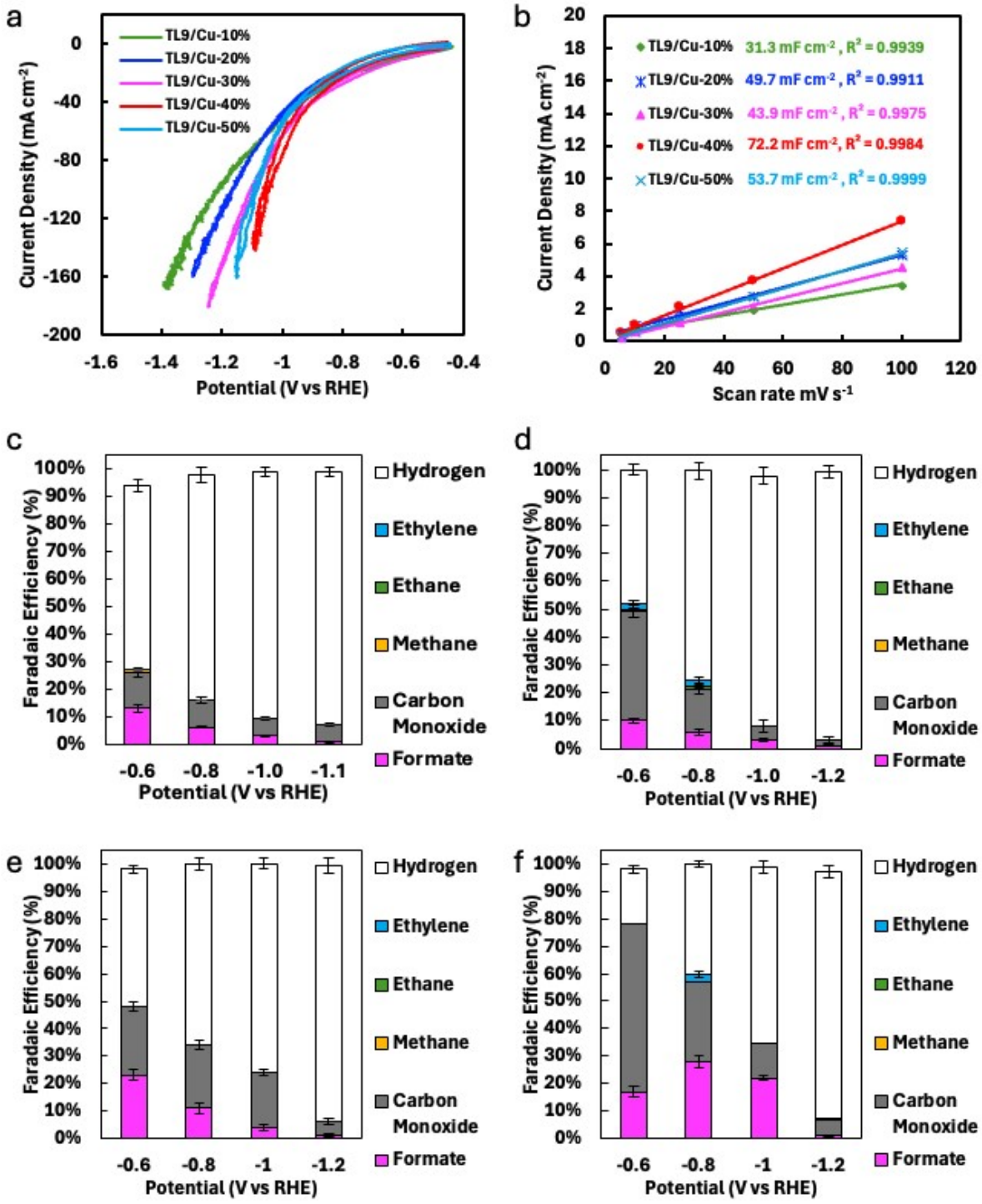

Figure S11. (a) Cyclic voltammograms and (b) double-layer capacitance (C_{dl}) of TL9/Cu composites with different Cu_2O loadings. Faradaic efficiencies of (c) TL9/Cu-10%, (d) TL9/Cu-20%, (e) TL9/Cu-30%, and (f) TL9/Cu-50% using H-type cell in 0.5 M $KHCO_3$ electrolyte saturated with CO_2 (pH = 7.4).

Table S5. Results of EIS fitting according to the equivalent circuit.

Element	TL9/Cu-40%	YEC/Cu-40%
R_s (Ω)	5.19	4.91
R_p (Ω)	3.43	2.80
CPE1 ($m\Omega^{-1}s^n$)	1.91	564×10^{-3}
n_{CPE1}	0.549	0.702
R_{ct} (Ω)	26	40
CPE2 ($\Omega^{-1}s^n$)	150	100
n_{CPE2}	1.05	0.6
W ($m\Omega^{-1}s^{0.5}$)	489	1.1×10^{15}

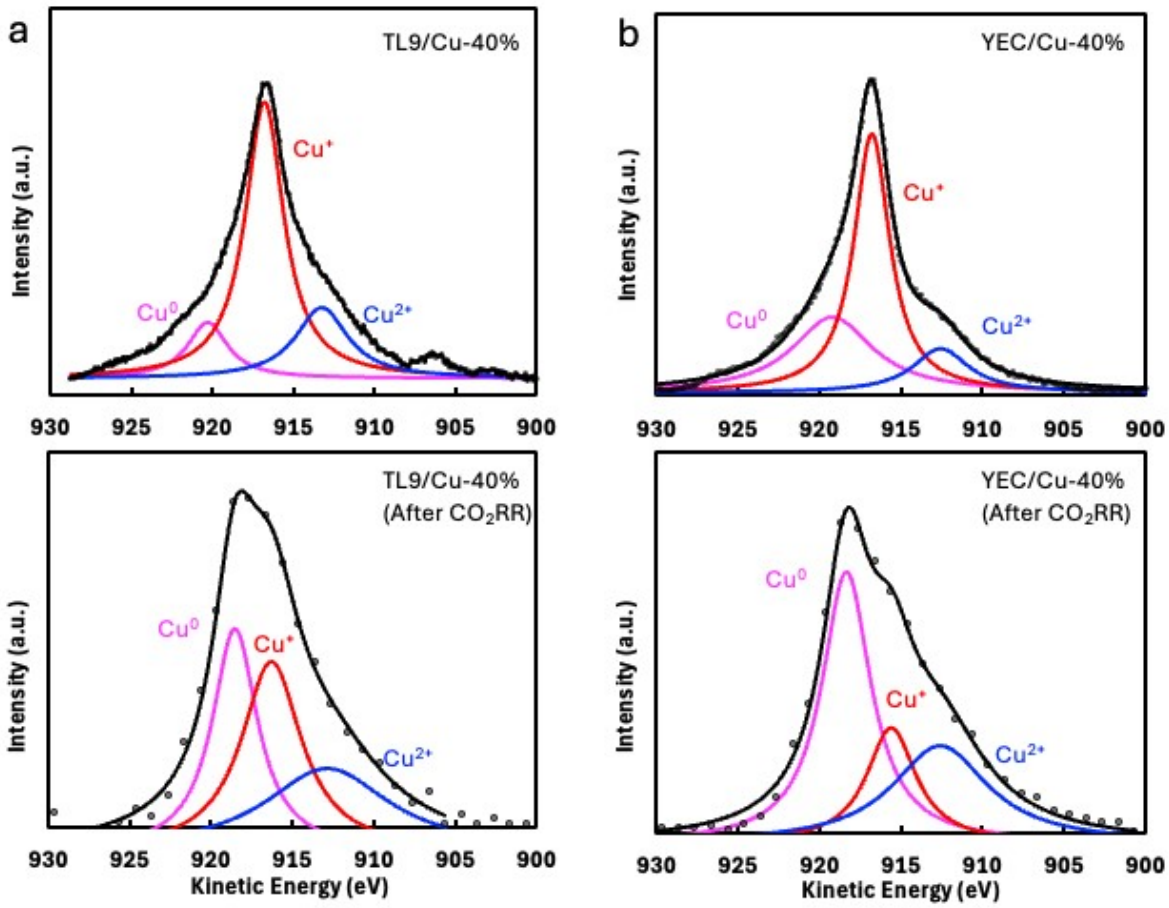

Figure S12. Cu LMM spectra of (a) TL9/Cu-40% and (b) YEC/Cu-40% before (top) and after (bottom) 24 hours of CO_2RR electrolysis at -0.6 V vs RHE using H-type cell in 0.5 M $KHCO_3$ electrolyte saturated with CO_2 (pH = 7.4).

Table S6. Relative composition of each Cu oxidation state determined from Cu LMM region of TL9/Cu-40% and YEC/Cu-40% before and after 24 hours of CO_2RR electrolysis at -0.6 V vs RHE using H-type cell in 0.5 M $KHCO_3$ electrolyte saturated with CO_2 (pH = 7.4).

Oxidation State	**Cu^0**		**Cu^+**		**Cu^{2+}**	
Sample	K.E. (eV)	Content (%)	K.E. (eV)	Content (%)	K.E. (eV)	Content (%)
TL9/Cu-40%	920.1	14%	916.8	64%	913.2	22%
TL9/Cu-40% (After CO_2RR)	918.3	32%	916.3	36%	912.9	33%
YEC/Cu-40%	919.2	34%	916.8	52%	912.6	14%
YEC/Cu-40% (After CO_2RR)	918.3	46%	916.0	20%	912.6	34%

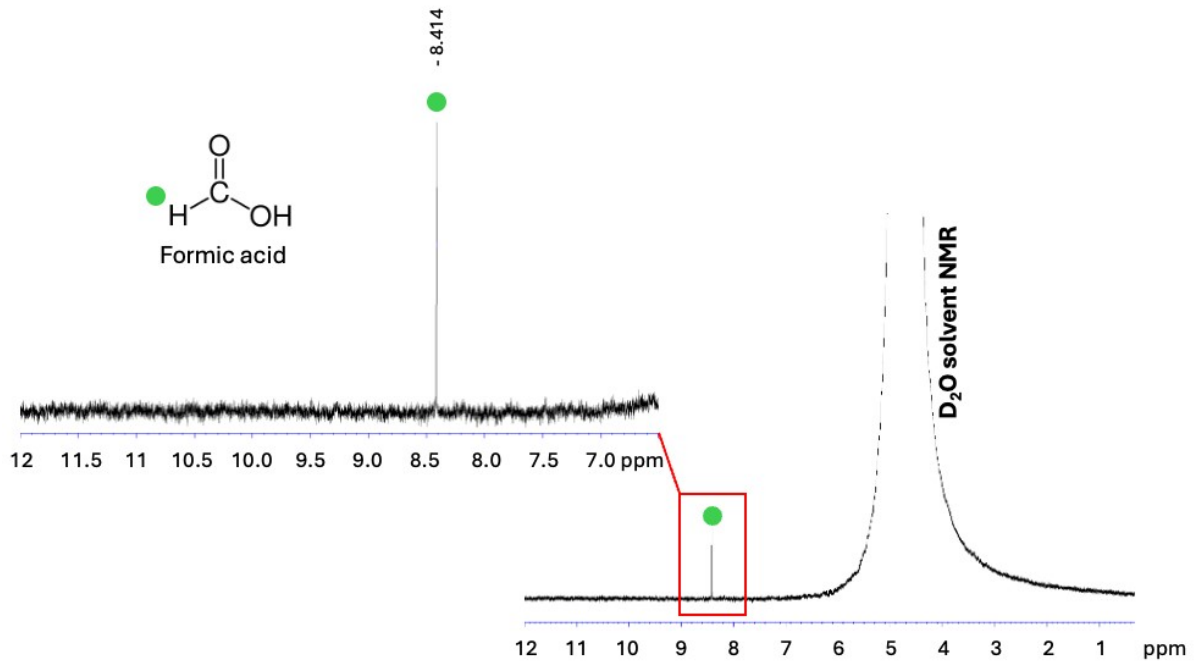

Figure S13. ^{1}H NMR spectrum of the post-CO_2RR electrolyte from working electrode chamber recorded in D_2O. The singlet at ~8.41 ppm corresponds to the formate proton ($HCOO^-$/HCOOH) (1).

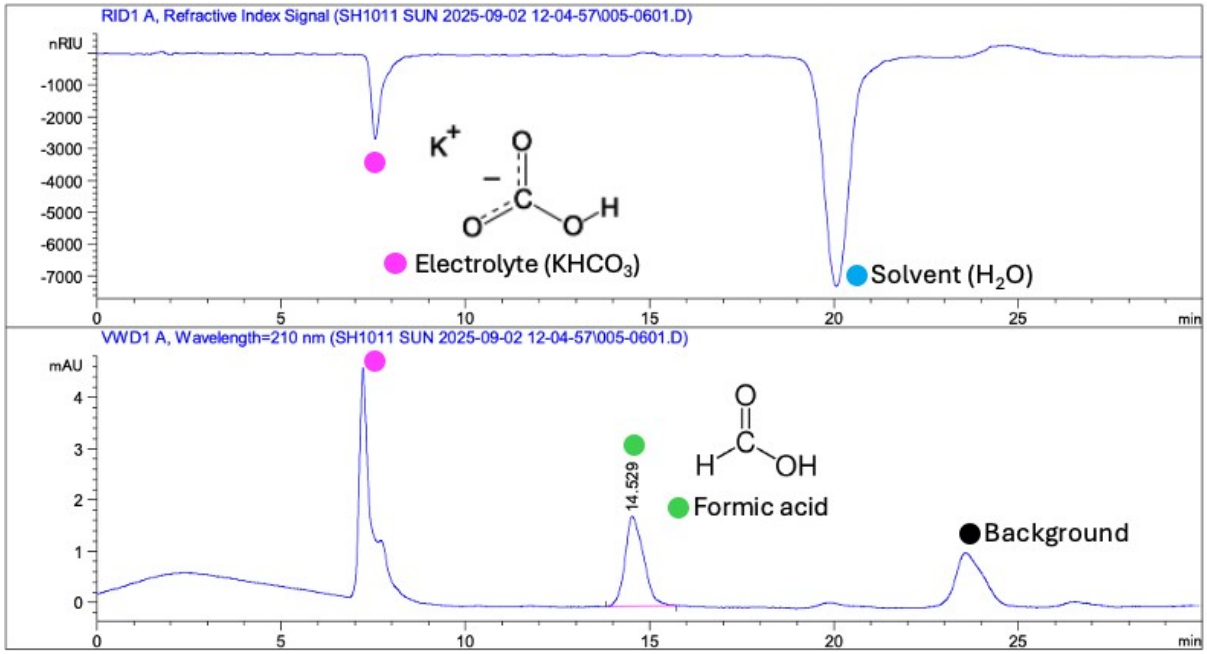

Figure S14. HPLC analysis of the liquid products after CO_2 electroreduction. The chromatograms obtained from RID (top) and UV detection at 210 nm (bottom) show a distinct peak at ~14.5 min, which matches the retention time of the formate standard,

confirming formate ($HCOO^-$/HCOOH) as the dominant liquid-phase product. The signal in both RID and UV detection at ~7.5 min were from the electrolyte (0.5 M $KHCO_3$). A large negative signal at ~20 min in the RID trace arises from the solvent (H_2O). A weak late-eluting feature at ~24 min observed in the UV trace is attributed to the electrolyte background after prolonged electrolysis (2, 3).

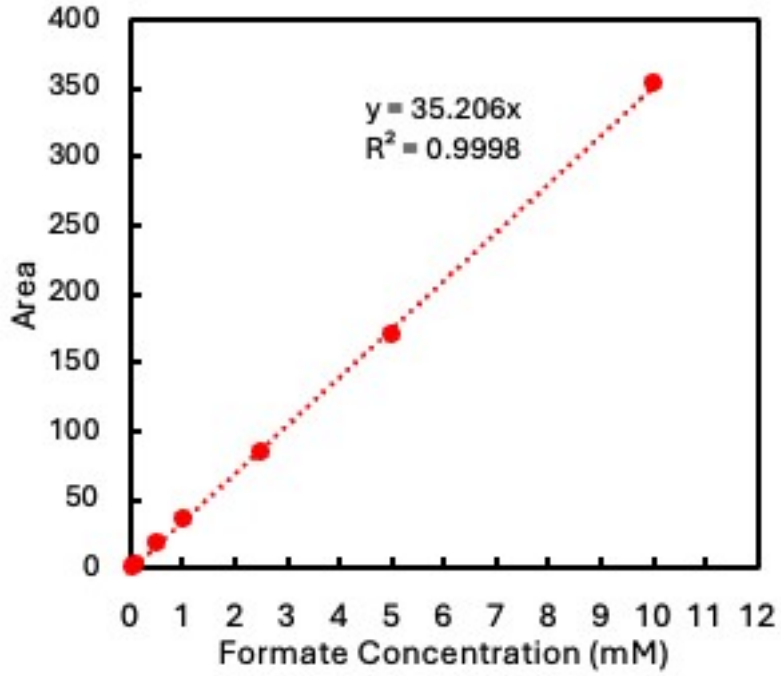

Figure S15. Calibration curve for formate quantification obtained by HPLC, showing a linear relationship between peak area and formate concentration.

References

1. Preikschas P, Martín AJ, Yeo BS, Pérez-Ramírez J. NMR-based quantification of liquid products in CO2 electroreduction on phosphate-derived nickel catalysts. Communications Chemistry 2023 6:1. 2023;6(1).

2. Verma S, Lu X, Ma S, Masel RI, Kenis PJA. The effect of electrolyte composition on the electroreduction of CO2 to CO on Ag based gas diffusion electrodes. Physical Chemistry Chemical Physics. 2016;18(10).

3. Marcandalli G, Monteiro MCO, Goyal A, Koper MTM. Electrolyte Effects on CO2 Electrochemical Reduction to CO. Accounts of Chemical Research. 2022;55(14).